Carbon Materials Hot Paper

DOI: 10.1002/ange.201409080

Graphitic Carbon Nitride Nanoribbons: Graphene-Assisted Formation and Synergic Function for Highly Efficient Hydrogen Evolution**

*Yang Zhao, Fei Zhao, Xiaopeng Wang, Chenyu Xu, Zhipan Zhang, Gaoquan Shi, and Liangti Qu**

Abstract: *The development of new promising metal-free catalysts is of great significance for the electrocatalytic hydrogen evolution reaction (HER). Herein, a rationally assembled three-dimensional (3D) architecture of 1D graphitic carbon nitride (g-C_3N_4) nanoribbons with 2D graphene sheets has been developed by a one-step hydrothermal method. Because of the multipathway of charge and mass transport, the hierarchically structured g-C_3N_4 nanoribbon–graphene hybrids lead to a high electrocatalytic ability for HER with a Tafel slope of 54 mV decade^{-1}, a low onset overpotential of 80 mV and overpotential of 207 mV to approach a current of 10 mA cm^{-2}, superior to those non-metal materials and well-developed metallic catalysts reported previously. This work presents a great advance for designing and developing highly efficient metal-free catalyst for hydrogen evolution.*

Hydrogen is believed to be the most promising clean energy and electrocatalytic hydrogen evolution reaction (HER) is one of the most important pathways to produce hydrogen from water.[1,2] The noble metals, platinum in particular, are the most effective HER electrocatalysts at present with high exchange current densities and small Tafel slopes.[3] However, due to the high price and the low abundance, researchers were inspired to use non-noble metals, metal composites, and even metal-free electrocatalysts for the HER. Examples include transition metals sulfides/nitrides/phosphides,[4–7] carbides,[8,9] and metal alloys,[10] for hydrogen evolution from water.[11] Unfortunately, most of the catalysts developed recently are based on the essential metal–H bond interaction for the HER, which commonly suffer from corrosion and passivation to the acidic proton exchange membrane electrolysis.[12] By contrast, the development of new promising non-metal HER electrocatalysts with high catalytic ability to replace metal-based counterparts still remains challenging.

[*] Y. Zhao, F. Zhao, X. Wang, C. Xu, Z. Zhang, Prof. L. Qu
Key Laboratory of Cluster Science, Ministry of Education
Beijing Key Laboratory of Photoelectronic/Electrophotonic Conversion Materials, School of Chemistry
Beijing Institute of Technology, Beijing 100081 (P. R. China)
E-mail: lqu@bit.edu.cn
Prof. G. Shi
Department of Chemistry, Tsinghua University
Beijing 100084 (P. R. China)

[**] We thank for financial support from the 973 program of China (grant number 2011CB013000) and NSFC (grant numbers 21325415, 21174019, and 51161120361), Fok Ying Tong Education Foundation (grant number 131043), and 111 Project (grant number 807012).

Supporting information for this article is available on the WWW under http://dx.doi.org/10.1002/anie.201409080.

Graphitic carbon nitride (g-C_3N_4) with a graphite-like structure has attracted considerable attention owing to its high in-plane nitrogen content, excellent chemical and thermal stability, appealing electronic structure, and environmental friendly feature, thus leading to multifunctional catalytic activities for photocatalysis, CO_2 reduction, and other energy conversion processes.[13–17,18] Due to the inherent low electronic conductivity and low surface area, g-C_3N_4 is mainly restricted to electrochemical-related applications. Graphene, a two-dimensional (2D) monolayer sheet of sp^2-bonded carbon atoms with fascinating properties such as a large specific surface area, outstanding electrical, mechanical, and thermal properties,[19] provides a solution to this problem. It was found that the combination of g-C_3N_4 with graphene could improve the conductivity and electrocatalytic performance of g-C_3N_4 for the oxygen reduction reaction (ORR),[20–22] oxygen evolution reaction,[23] and HER with catalytic activity even better than metal-based electrocatalysts.[24] Although much effort has been exclusively focused on the modification of g-C_3N_4 with conductive materials to promote its electronic and electrocatalytic behavior, little attention is paid to assembling the g-C_3N_4s into specifically nanostructured architectures[20,25] for highly efficient catalytic performance.

Herein, we achieve the rational assembly of 1D in situ formed g-C_3N_4 nanoribbons on 2D graphene sheets to form 3D interconnected networks (g-C_3N_4 nanoribbon-G) by a simple one-step hydrothermal method. Such hierarchical architecture of g-C_3N_4 nanoribbon-G provides a large accessible surface area, multi-electron transport channel and short diffusion distance for an excellent charge separation and transfer, that effectively accelerates the electrochemical process. As a result, the as-prepared g-C_3N_4 nanoribbon-G displays an excellent HER activity with a much low overpotential of 207 mV calibrated to reversible hydrogen electrode (RHE) to achieve a HER current density of 10 mA cm^{-2}, which are comparable to the existing well-developed metallic catalysts and superior to those non-metal HER catalysts reported previously (Tables S1 and S2), demonstrating the potential towards replacing the metal-based catalysts for highly efficient electrocatalysis of HER.

To prepare the g-C_3N_4 nanoribbon-G, a mixed suspension of g-C_3N_4 and graphene oxide (GO) with the weight ratio of 1/0.15 was hydrothermally treated in a Teflon-lined autoclave at 180 °C. During the treatment, the 3D graphene structure formed spontaneously.[26] Meanwhile, g-C_3N_4 preferred to nucleate at defects of GO, and assembled into g-C_3N_4 nanoribbons network on 3D graphene sheets (Figure 1a). As shown in Figure 1b, the prepared g-C_3N_4 nanoribbon-G

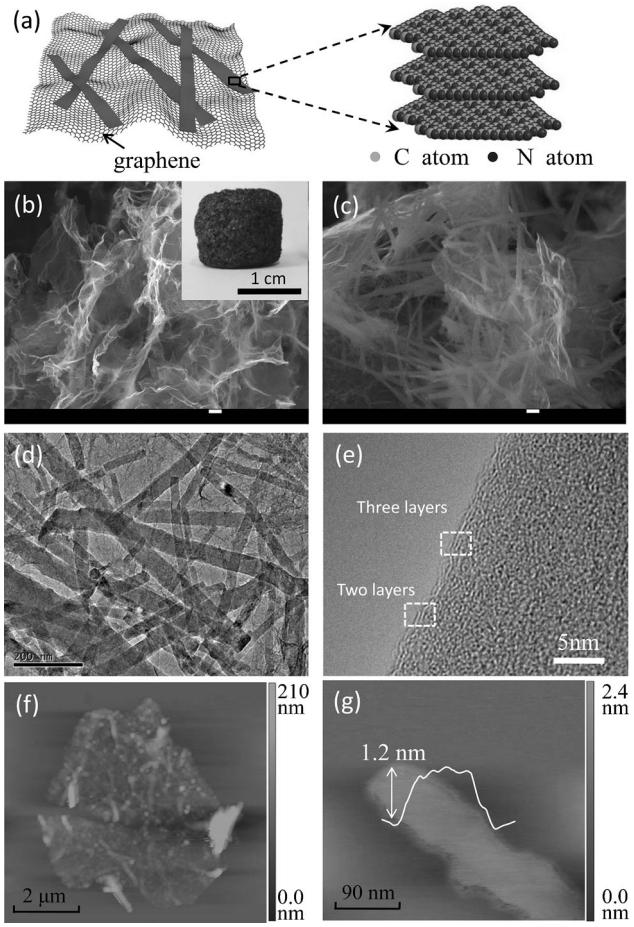

Figure 1. a) g-C_3N_4 nanoribbon-G and a possible structural model of the g-C_3N_4 nanoribbon. b,c) SEM images of the prepared g-C_3N_4 nanoribbon-G. The inset of (b) is a photo of the as-prepared g-C_3N_4 nanoribbon-G. d) TEM images of the prepared g-C_3N_4 nanoribbon-G, and e) a typical high-resolution TEM image of the g-C_3N_4 nanoribbon. f) AFM image of a graphene sheet with grown g-C_3N_4 nanoribbons. g) AFM image and height profile of a single g-C_3N_4 nanoribbon. Scale bars: b, 1 μm; c, 100 nm; d, 200 nm; e, 5 nm.

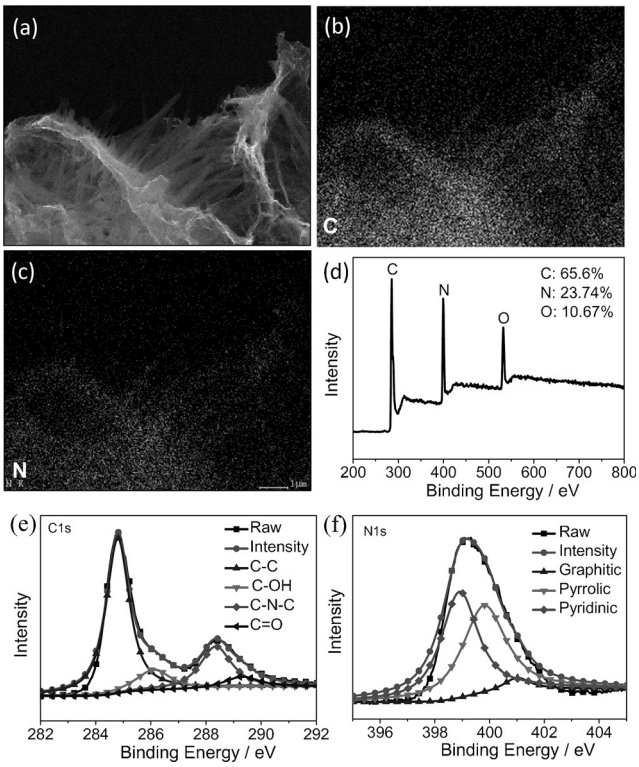

Figure 2. a) SEM image of g-C_3N_4 nanoribbon-G. b,c) The corresponding C- and N- elemental mappings. d) XPS spectrum of g-C_3N_4 nanoribbon-G. e,f) The corresponding high-resolution C1s and N1s peaks. Scale bars: a–c, 1 μm.

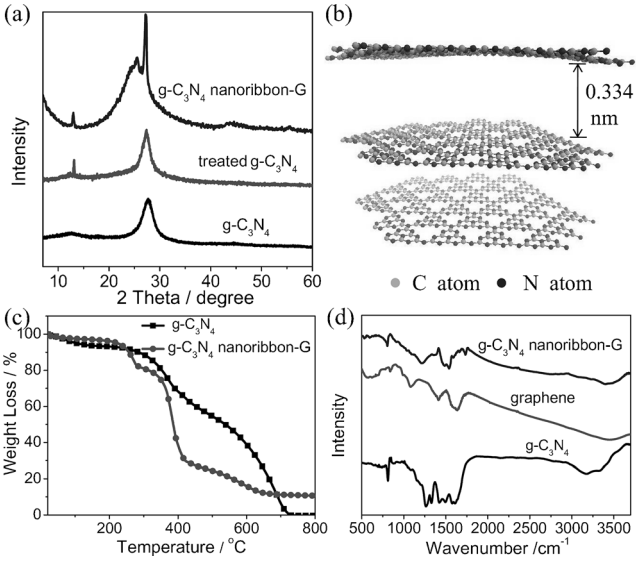

Figure 3. a) XRD patterns of the original g-C_3N_4, treated g-C_3N_4, and g-C_3N_4 nanoribbon-G and b) the corresponding structural model of the g-C_3N_4 nanoribbon. c) TGA curves of the original g-C_3N_4 and g-C_3N_4 nanoribbon-G in N_2 with a heating speed of 10 °C min^{-1}. d) FTIR spectrum of the original g-C_3N_4, graphene and g-C_3N_4 nanoribbon-G, respectively.

foam shows a loose 3D structure with a density of 20 mg cm^{-3} similar to that of common 3D graphene (see Figure S1 in the Supporting Information).[26] The enlarged SEM images reveal that g-C_3N_4 nanoribbons are randomly attached along graphene basal planes (Figure 1 c), as also verified by TEM in Figure 1 d. The high-resolution TEM exhibits g-C_3N_4 nanoribbon contains only a few layers of g-C_3N_4 sheets (Figure 1 e). The corresponding AFM image (Figure 1 f) revealed a typical topographic height of 1.2 nm (Figure 1 g), suggesting that the g-C_3N_4 nanoribbon consists of approximately three layers of g-C_3N_4 sheets consistent with TEM observation in Figure 1 e.

The elemental mappings revealed the coexistent and uniform distribution of C and N elements for the g-C_3N_4 nanoribbon-G (Figure 2 a–c), and the corresponding energy-dispersive spectrometry (EDS) was included in Figure S2a. X-ray photoelectron spectroscopy (XPS) measurements further verify the existence of a C 1s peak, along with an obvious N 1s peak corresponding to a N content of 23.74 at % and a weak O 1s peak without any impurities (Figure 2 d). The high-resolution C 1s spectrum is shown in Figure 2 e. The peak at 284.8 eV belongs to C-C coordination, and the peak centered at 288.3 eV corresponds to C-N coordination of g-C_3N_4. The

high-resolution N 1s spectrum (Figure 2 f) reveals the typical N status including pyridine-like (398.8 eV), pyrrolic (400.5 eV), and graphitic (401.1 eV) N species, which are also reflected by a C-N-C peak in the C 1s spectrum of g-C_3N_4 nanoribbon-G (Figure 2 e).The pressence of O elements with a content of approximately 10.7 at% probably comes from both reduced GO and g-C_3N_4 (Figure S2b and c).[26]

Figure 3 a shows the X-ray diffraction (XRD) patterns of g-C_3N_4 nanoribbon-G in comparison with original g-C_3N_4 and g-C_3N_4 samples treated by a hydrothermal method. The original g-C_3N_4 represents the typical diffraction peak at 27.3° corresponding to the (002) peak of g-C_3N_4 attributed to interlayer stacking reflection of conjugated aromatic systems. A weak broad peak at around 13° belongs to the (001) peak of g-C_3N_4 consistent with an in-plane structural motif.[16,27] With the hydrothermal treatment, the g-C_3N_4 shows a much sharper diffraction peaks at 13° than that of the initial g-C_3N_4, suggesting that the hydrothermal process favors the structure rearrangement of g-C_3N_4,[25] which is consistent with the SEM observation (Figure S3). Impressively, the g-C_3N_4 nanoribbon-G shows narrow diffraction peaks at 13° and a much sharper peak at 27.3° compared with other g-C_3N_4 samples, suggesting that graphene has induced the higher ordering structure of the planar tri-s-triazine units in g-C_3N_4s.[27,28a] The peak at approximately 25° observed in g-C_3N_4 nanoribbon-G belongs to the (002) peak of graphitic carbon planes. As shown in Figure 3 b, the *d* spacing of two stacking layers in the g-C_3N_4 nanoribbon obtained from XRD patterns is 0.334 nm, which is consistent with the TEM image (Figure 1 e) and slight more dense than the packing in crystalline graphite ($d =$ 0.34 nm).[13]

Thermogravimetric analysis (TGA) was performed to evaluate the thermal stability of the g-C_3N_4 nanoribbon-G. The weight loss of less than 10% at temperatures of up to 200 °C is ascribed to the removal of physically adsorbed water (Figure 3 c). The fast mass loss at 310 and 400 °C and a gradually weight loss from 400 to 650 °C can be attributed to a loss in tri-s-triazine-based units or other advanced condensates, which is similar with those nanoscale C_3N_4 structures.[28b] Compared to the original g-C_3N_4, the weight of g-C_3N_4 nanoribbon-G remains stables after 650 °C, indicating the improved thermal stability of the products.[29] The g-C_3N_4 nanoribbon-G was further characterized by FTIR spectroscopy (Figure 3 d and Figure S4a). g-C_3N_4 shows typical C-N heterocyclic stretches of the triazine ring in the 1100–1700 cm^{-1} region. The sharp absorption at approximately 800 cm^{-1} belongs to the deformation of tri-s-triazine ring modes. The peaks at approximately 3200 and 3400 cm^{-1} are attributed to stretching and deformation modes of -NH_2 groups.[30] Although most of the characteristic peaks of CN heterocycles in g-C_3N_4 of the prepared sample are overlapped by graphene, the peaks at 800 and 1571 cm^{-1} belongi to g-C_3N_4 can still be recognized.

The HER activities of g-C_3N_4 nanoribbon-G were investigated in 0.5 M sulfuric acid electrolyte using a three-electrode setup with a sample loading of 0.143 mg cm^{-2} on a glassy carbon (GC) electrode and polarization curves at different loading weight are also shown in Figure S4b and c. The original g-C_3N_4 and N-doped graphene (N-G) materials were also studied for comparison (Figure S5b–d). As shown in Figure 4 a, the prepared g-C_3N_4 nanoribbon-G exhibits a much lower onset overpotential ($\eta = 80$ mV) than other carbon-based materials and even non-noble metals or oxides (Table S1),[4,5,31,32] suggesting a superior HER activity. On the other hand, the g-C_3N_4 nanoribbon-G shows a large cathodic current density of 23.7 mA cm^{-2} at $\eta = 300$ mV, which is about 100 times that of the N-G electrode (0.24 mA cm^{-2}) and far bigger than the original g-C_3N_4 electrode (0.04 mA cm^{-2}; Figure 4 a). The Tafel slope of g-C_3N_4 nanoribbon-G was 54 mV dec^{-1}, indicating that the release of molecular hydro-

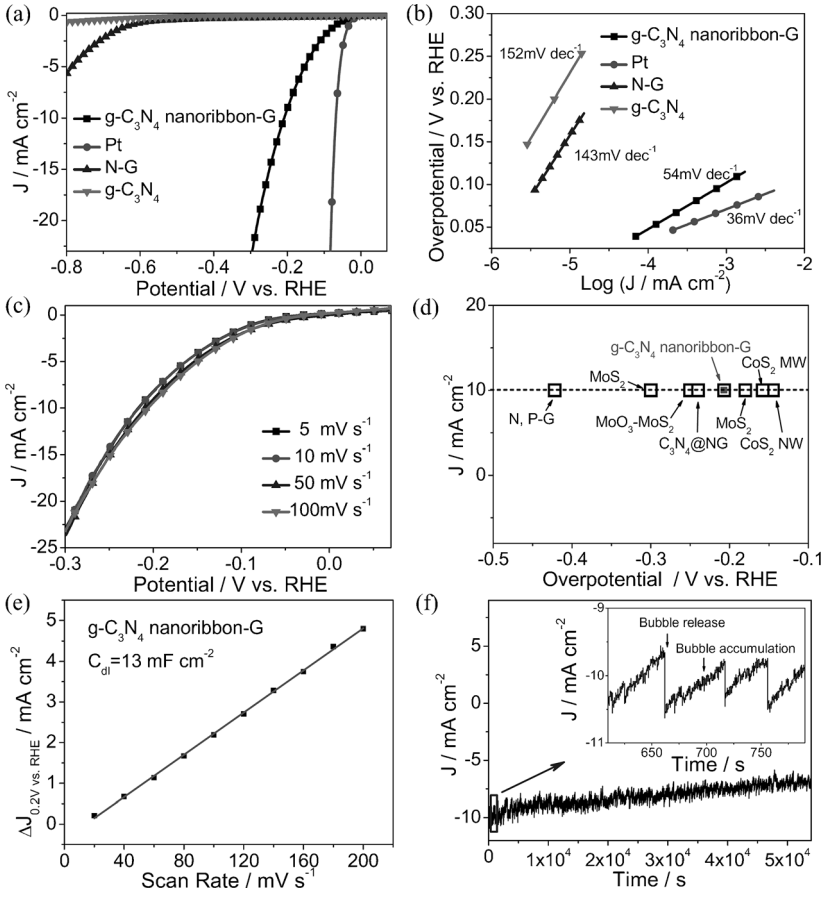

Figure 4. a) The HER polarization curves and b) the corresponding Tafel plots of various catalysts (g-C_3N_4 nanoribbon-G, Pt wire, N-G and g-C_3N_4, respectively) with a scan rate of 50 mV s^{-1} in 0.5 M H_2SO_4. c) The polarization curves of g-C_3N_4 nanoribbon-G with a scan rate from 5 to 100 mV s^{-1}. d) The HER current density at 10 mA cm^{-2} versus overpotential for various catalysts. e) Plot showing the extraction of the double layer capacitance (Cdl) for g-C_3N_4 nanoribbon-G at 0.2 V. f) Time dependence of the current density at 200 mV versus RHE.

gen is the rate-limiting step (see section SI-A in the Supporting Information),[4] thus leading to a faster increment of the HER rate with increasing overpotential (Figure 4a,b and Table S1). As shown in Figure 4c, the *i–V* curves of g-C_3N_4 nanoribbon-G are almost the same at scan rates from 10 to 100 mV s^{-1}, demonstrating its excellent stability for highly active electrochemical process. The polarization curve recorded on g-C_3N_4 nanoribbon-G displays an ultra-low overpotential of 207 mV to achieve a 10 mA cm^{-2} HER current density, which is more positive than those of non-metal catalysts and comparable to metallic derivatives (Figure 4a&d and Table S1).[24,31–33] On the other hand, the exchange current density (J_o) of g-C_3N_4 nanoribbon-G obtained by applying an extrapolation method to the Tafel plot was 39.8 μF cm^{-2}, which is far larger than other compared metal-free catalysts, well-developed non-noble metal nanomaterials, and their derivatives after normalizing them to the same surface area and catalyst loading mass (Table S2).[4,24,31–35]

The electrochemical double layer capacitance (Cdl) was carried out using a simple cyclic voltammetry (CV) method to estimate the effective surface areas of the solid–liquid interface for g-C_3N_4 nanoribbon-G (Figure 4e, Figure S6a, and Table S2).[24,36a] For capacitance measurement, a potential range of 0.15–0.25 V versus RHE was selected owing to a negligible Faradic current features in this region for g-C_3N_4 nanoribbon-G. The g-C_3N_4 nanoribbon-G exhibits very high Cdl of 13 mF cm^{-2} compared with other counterparts, indicating the highly exposed active site and excellent HER (Table S2). Besides, the LSV plots of g-C_3N_4 nanoribbon-G at different scan rates after subtracting the capacitance currents were also demonstrated in Figure S6b. Continuous HER at a constant overpotential was conducted to investigate the durability of g-C_3N_4 nanoribbon-G. As demonstrated in Figure 4f, a typical serrate shape was observed for g-C_3N_4 nanoribbon-G at an overpotential of 200 mV because of the alternate accumulation and release processes of H_2 (g) bubbles. The current density exhibits only a slight degradation after long-term cycling of 54000 seconds, probably because of the consumption of H^+ or the accumulation of H_2 bubbles on the electrode surface that hinder the reaction process (Figure 4f and Figure S7).

The mechanism for converting H^+ to H_2 during HER in acidic medium have been proposed.[4,36b] The high HER activity and excellent stability of the prepared g-C_3N_4 nanoribbon-G can be attributed to three aspects: 1) The g-C_3N_4 nanoribbon with unique 1D structure not only provides highly active hydrogen binding sites during the HER process,[24] but also facilitates inter-electron transport along the basal surfaces of g-C_3N_4. 2) The in situ formed 1D g-C_3N_4 nanoribbon on 3D graphene framework can reinforce the intimate contact and excellent electrical connection between g-C_3N_4 nanoribbon and graphene, leading to an enhanced electron transfer from graphene to the g-C_3N_4 nanoribbon and further accelerating the HER process (Figure 1d and e). 3) The disordered distributions of the g-C_3N_4 nanoribbon on graphene, just like a "grid" covered in graphene sheets, offers large amounts of intervals, which can fully infiltrate with the electrolyte and in certain extent, the "grid" can improve bubble convection and release away from the electrode surface preventing the H_2 (g) bubbles from damaging the catalysts during the accumulation process, thus leading to a much long-term stability of g-C_3N_4 nanoribbon-G electrodes. In general, the unique 3D assembled architecture of 1D g-C_3N_4 nanoribbons combined with 2D graphene sheets provides a new metal-free catalyst for highly efficient electrocatalytic hydrogen evolution.

The g-C_3N_4 nanoribbons are generally not produced if the GO suspension is absent during the hydrothermal process. To investigate the formation of the 1D g-C_3N_4 nanoribbon on the 2D graphene sheets, we tracked the growth of the g-C_3N_4 nanoribbon with reacting time (Figure 5). During the hydrothermal treatment, the hydrogen bonds within the bulk g-C_3N_4 sheets could be breakable because of the enhanced solvation at elevated temperatures, leading to the conversion of bulk g-C_3N_4 to molecule-like g-C_3N_4 (Figure S8). These molecule-like g-C_3N_4s could first nucleate at the "active sites" (such as functional groups, defects or folds) of GO nanosheets at the beginning of the hydrothermal process (Figure 5a and b). The "active sites" would minimize the interfacial energy barrier between the solid surface and liquid solution, which was beneficial to the subsequent assembly of g-C_3N_4 on them. With the increase of reaction time, thin and fine strips of g-C_3N_4s were formed (Figure 5c and d). Finally, dense g-C_3N_4 nanoribbon networks were generated on graphene sheets with the prolonged hydrothermal reaction (Figure 5e and f).

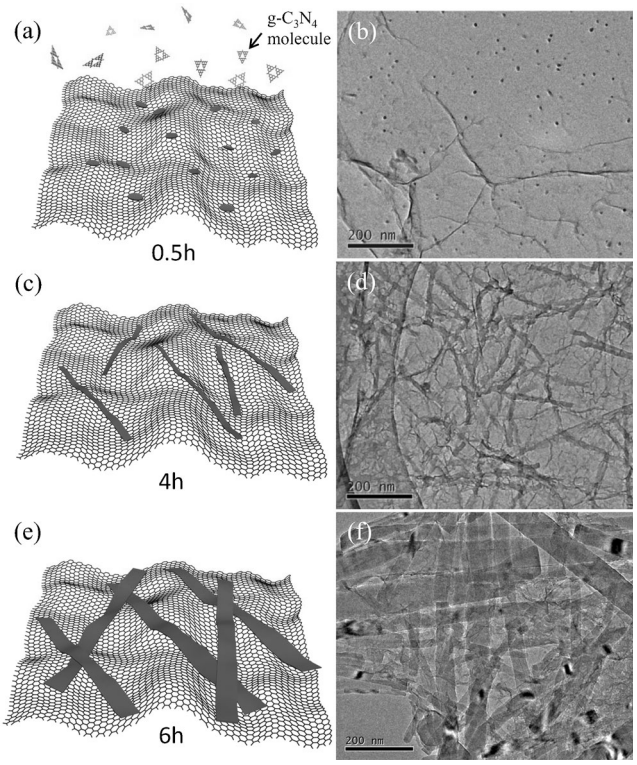

Figure 5. Nucleation and growth process of g-C_3N_4 nanoribbons on graphene with the g-C_3N_4/GO weight ratio of 1/0.15. The mixture of g-C_3N_4 and GO suspensions were hydrothermally treated at 180 °C for 0.5 (a,b), 4 (c,d), and 6 h (e,f), respectively.

Interestingly, a longer reaction time (e.g., 24 h) could lead to the formation of g-C_3N_4 rods across the graphene networks (Figure S9), which suggests the convenience of the hydrothermal approach for tuning the nanostructure of g-C_3N_4. In addition, the reacting temperature and the weight ratio of g-C_3N_4 versus GO are also important to affect the formation of g-C_3N_4 nanoribbons. The detailed discussion has been included in Figures S10–S13.

In summary, the rationally assembled 3D architecture of in situ formed 1D g-C_3N_4 nanoribbons with 2D graphene sheets has been achieved by using a simple one-step hydrothermal method, which exhibits highly efficient electrocatalytic ability for the HER with low overpotential and extremely large exchange current density, comparable to or even better than that of the existing metal-free and well-fabricated metallic catalysts. The formation of g-C_3N_4 nanoribbons on graphene sheets is controllable by tuning the reaction parameters. This work opens the opportunity for constructing the new type of g-C_3N_4 nanostructured materials for a large variety of electronic and photoelectronic device applications beyond the highly efficient catalytic behavior for the HER demonstrated in this study.

Received: September 13, 2014
Published online: November 7, 2014

Keywords: carbon · electrocatalysis · graphene · hydrogen evolution · nanoribbons

[1] H. I. Karunadasa, C. J. Chang, J. R. Long, *Nature* **2010**, *464*, 1329 – 1333.
[2] G. W. Crabtree, M. S. Dresselhaus, M. V. Buchanan, *Phys. Today* **2004**, *57*, 39 – 44.
[3] B. E. Conway, B. V. Tilak, *Electrochim. Acta* **2002**, *47*, 3571 – 3594.
[4] J. F. Xie, J. Zhang, S. Li, F. Grote, X. Z. Zhang, H. Zhang, R. Wang, Y. Lei, B. Pan, Y. Xie, *J. Am. Chem. Soc.* **2013**, *135*, 17881 – 17888.
[5] J. F. Xie, H. Zhang, S. Li, R. Wang, X. Sun, M. Zhou, J. Zhou, X. W. (David) Lou, Y. Xie, *Adv. Mater.* **2013**, *25*, 5807 – 5813.
[6] a) D. Voiry, H. Yamaguchi, J. Li, R. Silva, D. C. B. Alves, T. Fujita, M. Chen, T. Asefa, V. B. Shenoy, G. Eda, M. Chhowalla, *Nat. Mater.* **2013**, *12*, 850 – 855; b) W.-F. Chen, K. Sasaki, C. Ma, A. I. Frenkel, N. Marinkovic, J. T. Muckerman, Y. M. Zhu, R. R. Adzic, *Angew. Chem. Int. Ed.* **2012**, *51*, 6131 – 6135; *Angew. Chem.* **2012**, *124*, 6235 – 6239.
[7] a) J. Tian, Q. Liu, A. M. Asiri, X. Sun, *J. Am. Chem. Soc.* **2014**, *136*, 7587 – 7590; *Angew. Chem. Int. Ed.* **2014**, *53*, 9577 – 9581; b) Z. Pu, Q. Liu, C. Tang, A. M. Asiriand, X. Sun, *Nanoscale* **2014**, *6*, 11031 – 11034; c) Q. Liu, J. Tian, W. Cui, P. Jiang, N. Cheng, A. M. Asiri, X. Sun, *Angew. Chem. Int. Ed.* **2014**, *53*, 6710 – 6714; *Angew. Chem.* **2014**, *126*, 6828 – 6832; d) Z. Xing, Q. Liu, A. M. Asiri, X. Sun, *Adv. Mater.* **2014**, *26*, 5702 – 5707; e) Z. Pu, Q. Liu, P. Jiang, A. M. Asiri, A. Y. Obaid, X. Sun, *Chem. Mater.* **2014**, *26*, 4326 – 4329; f) E. J. Popczun, C. G. Read, C. W. Roske, N. S. Lewis, R. E. Schaak, *Angew. Chem. Int. Ed.* **2014**, *53*, 5427 – 5430; *Angew. Chem.* **2014**, *126*, 5531 – 5534.
[8] H. Vrubel, X. Hu, *Angew. Chem. Int. Ed.* **2012**, *51*, 12703; *Angew. Chem.* **2012**, *124*, 12875.
[9] D. V. Esposito, S. T. Hunt, A. L. Stottlemyer, B. E. McCandless, R. W. Birkmire, J. G. Chen, *Angew. Chem.* **2010**, *49*, 9859 – 9862; *Angew. Chem.* **2010**, *122*, 10055 – 10058.
[10] J. Greeley, T. F. Jaramillo, J. Bonde, I. Chorkendorff, J. K. Nørskov, *Nat. Mater.* **2006**, *5*, 909 – 913.
[11] R. Subbaraman, D. Tripkovic, K. C. Chang, D. Strmcnik, A. P. Paulikas, P. Hirunsit, M. Chan, J. Greeley, V. Stamenkovic, N. M. Markovic, *Nat. Mater.* **2012**, *11*, 550 – 557.
[12] E. J. Popczun, J. R. McKone, C. G. Read, A. J. Biacchi, A. M. Wiltrout, N. S. Lewis, R. E. Schaak, *J. Am. Chem. Soc.* **2013**, *135*, 9267 – 9270.
[13] Y. Zheng, J. Liu, J. Liang, M. Jaroniec, S. Z. Qiao, *Energy Environ. Sci.* **2012**, *5*, 6717 – 6731.
[14] M. Groenewolt, M. Antonietti, *Adv. Mater.* **2005**, *17*, 1789 – 1792.
[15] X. C. Wang, K. Maeda, X. F. Chen, K. Takanabe, K. Domen, Y. D. Hou, X. Z. Fu, M. Antonietti, *J. Am. Chem. Soc.* **2009**, *131*, 1680 – 1681.
[16] Y. Hou, Z. H. Wen, S. M. Cui, X. Guo, J. H. Chen, *Adv. Mater.* **2013**, *25*, 6291 – 6297.
[17] a) J. Xu, Y. J. Wang, Y. F. Zhu, *Langmuir* **2013**, *29*, 10566 – 10572; b) S. Yang, Y. Gong, J. Zhang, L. Zhan, L. Ma, Z. Fang, R. Vajtai, X. C. Wang, P. M. Ajayan, *Adv. Mater.* **2013**, *25*, 2452 – 2456; c) F. Goettmann, A. Thomas, M. Antonietti, *Angew. Chem. Int. Ed.* **2007**, *46*, 2717 – 2720; *Angew. Chem.* **2007**, *119*, 2773 – 2776.
[18] a) N. Cheng, J. Tian, Q. Liu, C. Ge, A. H. Qusti, A. M. Asiri, A. O. Al-Youbi, X. Sun, *ACS Appl. Mater. Interfaces* **2013**, *5*, 6815 – 6819; b) J. Tian, Q. Liu, A. M. Asiri, A. H. Qusti, A. O. Al-Youbi, X. Sun, *Nanoscale* **2013**, *5*, 11604 – 11609.
[19] a) K. Geim, K. S. Novoselov, *Nat. Mater.* **2007**, *6*, 183 – 191; b) K. S. Novoselov, A. K. Geim, S. V. Morozov, D. Jiang, Y. Zhang, S. V. Dubonos, I. V. Grigorieva, A. A. Firsov, *Science* **2004**, *306*, 666 – 669.
[20] J. Liang, Y. Zheng, J. Chen, J. Liu, D. Hulicova-Jurcakova, M. Jaroniec, S. Z. Qiao, *Angew. Chem. Int. Ed.* **2012**, *51*, 3892 – 3896; *Angew. Chem.* **2012**, *124*, 3958 – 3962.
[21] S. B. Yang, X. L. Feng, X. C. Wang, K. Müllen, *Angew. Chem. Int. Ed.* **2011**, *50*, 5339 – 5343; *Angew. Chem.* **2011**, *123*, 5451 – 5455.
[22] J. Q. Tian, R. Ning, Q. Liu, A. M. Asiri, A. O. Al-Youbi, X. Sun, *ACS Appl. Mater. Interfaces* **2014**, *6*, 1011 – 1017.
[23] T. Y. Ma, J. R. Ran, S. Dai, M. Jaroniec, S. Z. Qiao, *Angew. Chem. Int. Ed.* **2014**, *53*, 7281 – 7285; *Angew. Chem.* **2014**, *126*, 7409 – 7413.
[24] Y. Zheng, Y. Jiao, Y. Zhu, L. H. Li, Y. Han, Y. Chen, A. Du, M. Jaroniec, S. Z. Qiao, *Nat. Commun.* **2014**, *5*, 3783 – 3791.
[25] Y. S. Jun, J. Park, S. U. Lee, A. Thomas, W. H. Hong, G. D. Stucky, *Angew. Chem. Int. Ed.* **2013**, *52*, 11083 – 11087; *Angew. Chem.* **2013**, *125*, 11289 – 11293.
[26] a) Y. X. Xu, K. Sheng, C. Li, G. Shi, *ACS Nano* **2010**, *4*, 4324 – 4330; b) Y. Zhao, J. Liu, Y. Hu, H. Cheng, C. Hu, C. Jiang, L. Jiang, A. Y. Cao, L. T. Qu, *Adv. Mater.* **2013**, *25*, 591 – 595.
[27] a) P. Niu, L. Zhang, G. Liu, H. M. Cheng, *Adv. Funct. Mater.* **2012**, *22*, 4763 – 4770; b) X. C. Wang, K. Maeda, A. Thomas, K. Takanabe, G. Xin, J. M. Carlsson, K. Domen, M. Antonietti, *Nat. Mater.* **2013**, *8*, 76 – 80; c) Y. J. Cui, Z. Ding, X. Fu, X. C. Wang, *Angew. Chem. Int. Ed.* **2012**, *51*, 11814 – 11818; *Angew. Chem.* **2012**, *124*, 11984 – 11988.
[28] a) J. Zhang, G. Zhang, X. Chen, S. Lin, L. Möhlmann, G. Dołęga, G. Lipner, M. Antonietti, S. Blechert, X. Wang, *Angew. Chem. Int. Ed.* **2012**, *51*, 3183 – 3187; *Angew. Chem.* **2012**, *124*, 3237 – 3241; b) Y. C. Zhao, Z. Liu, W. Chu, L. Song, Z. Zhang, D. Yu, Y. Tian, S. Xie, L. F. Sun, *Adv. Mater.* **2008**, *20*, 1777 – 1781.
[29] Y. Zhang, J. Ge, L. Wang, D. Wang, F. Ding, X. Tao, W. Chen, *Sci. Rep.* **2013**, *3*, 2771 – 2779.
[30] a) D. Foy, G. Demazeau, P. Florian, D. Massiot, C. Labrugère, G. Goglio, *J. Solid State Chem.* **2009**, *182*, 165 – 171; b) X. Li, J. Zhang, L. Shen, Y. Ma, W. Lei, Q. Cui, G. Zou, *Appl. Phys. A* **2009**, *94*, 387 – 392.
[31] Z. Chen, D. Cummins, B. N. Reinecke, E. Clark, M. K. Sunkara, T. F. Jaramillo, *Nano Lett.* **2011**, *11*, 4168 – 4175.

[32] J. Kibsgaard, Z. Chen, B. N. Reinecke, T. F. Jaramillo, *Nat. Mater.* **2012**, *11*, 964 – 969.
[33] Y. Zheng, Y. Jiao, L. H. Li, T. Xing, Y. Chen, M. Jaroniec, S. Z. Qiao, *ACS Nano* **2014**, *8*, 5290 – 5296.
[34] L. Liao, J. Zhu, X. Bian, L. Zhu, M. Scanlon, H. H. Girault, B. Liu, *Adv. Funct. Mater.* **2013**, *23*, 5326 – 5333.
[35] D. Merki, H. Vrubel, L. Rovelli, S. Fierro, X. Hu, *Chem. Sci.* **2012**, *3*, 2515 – 2525.
[36] a) M. A. Lukowski, A. S. Daniel, F. Meng, A. Forticaux, L. Li, S. Jin, *J. Am. Chem. Soc.* **2013**, *135*, 10274; b) A. B. Laursen, S. Kegnæs, S. Dahl, I. Chorkendorff, *Energy Environ. Sci.* **2012**, *5*, 5577 – 5591.

